

# Speed Sensor-Aided Navigation Filter for Robust Localization in GNSS-Denied Mining Environments

David Benz\* | Jan-Jöran Gehrt | René Zweigel | Dirk Abel

Institute of Automatic Control, RWTH Aachen, Germany

## Correspondence

David Benz  
Campus-Boulevard 30  
52074 Aachen, Germany  
Email: [d.benz@irt.rwth-aachen.de](mailto:d.benz@irt.rwth-aachen.de)

## Abstract

The automation of mining haulage vehicles has great potential in terms of safety and economy. The performance of autonomous vehicles depends largely on highly accurate vehicle state information. Deep mines are especially challenging, as satellite-based localization methods are reaching their limits. Therefore, we introduce a new navigation filter concept for the precise and robust localization of the haulage fleet that can handle temporary GNSS interruptions in deep open-pit mines. The multi-sensor navigation filter utilizes an inertial measurement unit and is aided by GNSS. We introduce a new optical speed sensor update within the tightly coupled unscented Kalman filter. The speed sensor measures the slip-free two-dimensional speed above ground. The filter was validated with an articulated dumper in a gravel pit. The new filter achieved a mean position error of 0.24 m during a test drive of 190 s with a simulated GNSS outage of 90 s.

## Keywords

autonomous dump truck, inertial navigation, mining, odometry, satellite-based navigation, state estimation

## 1 | INTRODUCTION

Supplying industry with important raw materials while reducing the impact on nature will become increasingly important in the future. A mixed mine operation, i.e., underground and surface mining in a hybrid form, is promising. Automating all vehicles involved can further increase productivity, sustainability, and safety. Autonomous transport units can operate reliably around the clock, even in dangerous areas for employees. Sustainability and safety increase by making more intensive use of existing mines as autonomous vehicles can operate in safety-critical areas.

A robust and accurate vehicle localization is one of the most challenging tasks towards autonomous mining, as satellite-based localization methods are reaching their limits in deep mines. Autonomous transport units have high demands on vehicle state estimation to enable safe travel along the often narrow paths in mines. In addition, automated loading and unloading maneuvers require precise positioning and alignment of the vehicles. Current research focuses on the automation of mining processes, machine-to-machine communication, vehicle localization, and vehicle control.

This publication addresses the challenge of locating vehicles in deep open-pit mines where temporary GNSS outages might occur. For most types of vehicles and applications, coupling inertial measurements and GNSS observables is a suitable approach for self-localization (Konrad et al., 2018). Open-pit mines represent a constantly changing environment. Deep funnel-shaped mines reduce the sky-view angle from a certain position onward so that only a few, if any, GNSS signals are received. Uneven surfaces with potholes and the vehicle's vibration will lead to the fact that a position solution only based on inertial measurements will no longer meet the required accuracies after only a few seconds. The reason for this is the double integration of noisy acceleration data, which causes even the smallest errors to grow strongly over time and make position determination impossible. Therefore, a localization approach only aided by GNSS cannot satisfy the requirements for guidance and control of mining machines. Odometry is a well-known localization method. However, no studies are known to us that cover wheel encoders or velocity sensors like Doppler radar in combination with articulated dump trucks to cover GNSS-denied environments. Therefore, we propose a novel approach to solve the localization problem in open-pit mines. The main contributions of this publication are as follows:

1. We propose a multi-sensor navigation filter that fuses IMU, GNSS, and lateral and longitudinal speed measurements.
2. We present the corresponding speed sensor measurement model that has inherently nonholonomic constraints and estimates and compensates for the sensor misalignment angle.
3. We evaluate the approach with an articulated dumper on tarmac and in a gravel pit with simulated GNSS interruptions. Our approach achieves a mean 2D position error of 0.24 m on a test drive with a simulated GNSS interruption of 90 s.

The publication on hand describes the further development of a tightly coupled navigation filter presented in former publications (Breuer et al., 2016; Gehrt et al., 2018; Konrad et al., 2018). It is part of the development of the *Autonomes Robustes Transportsystem für hybride Umweltschonende Rohstoffgewinnung auf basis knickgelenker Sonderfahrzeuge (ARTUS)* research project, in which an autonomous transport fleet is being developed for use in hybrid mines. This publication is structured as follows: First, related work is introduced and discussed. Subsequently, the basis navigation filter is explained, and the optical speed sensor is presented, including the measurement principle, measurement model, and misalignment angle estimation. The GNSS preprocessing, filter parametrization, and initialization are described afterward. Then the measurement setup is described, and the experimental results from a parking lot and a gravel pit are evaluated and discussed. Finally, a conclusion and outlook on future developments are given.

## 2 | RELATED WORK

This section presents approaches that address localization in the presence of temporary GNSS interruptions. One solution is to extend the navigation system by further aiding sensors that achieve sufficient localization accuracy in GNSS-denied environments. Wheel odometry is a possible solution but is accompanied by several complex uncertainties. The transmission of drive forces via the tires is always associated with slip. Furthermore, the tire size or pressure can change. The measurement of the vehicle speed via rotary encoders on the axles leads to non-negligible measurement errors that negatively affect position determination. This phenomenon

can be observed especially on driven wheels or, in the case of articulated vehicles, presumably on all wheels (Groves, 2013). Scheduling et al. (1999) is the only study known to us in which odometry is considered for the navigation task of an articulated vehicle. However, the authors only use the measured articulation angle in their approach, rather than wheel encoders.

Other possible aiding sensors measuring the vehicle velocity are Doppler radars. Yang et al. (2021) investigate the use of a Doppler radar combined with a strapdown inertial navigation system and wheel odometry for land vehicle navigation. The authors thereby use the Doppler radar only to get the longitudinal velocity. As no absolute position updates are performed with, e.g., GNSS, the position error is too high for precise maneuvering of mining vehicles. Furthermore, a single Doppler radar can only measure one velocity component, which reduces the benefit of the radar sensor beside the wheel odometry. Determining the 2D vehicle velocity by an arbitrary number of Doppler radars is presented by Kellner et al. (2014). Their approach can estimate longitudinal and lateral velocity by combining measurements of different Doppler radars mounted on a vehicle. The sensors are arranged horizontally, and the vehicle motion is determined based on the objects moving relative to the vehicle, such as trees. The authors achieved great results in urban scenarios where lots of objects are in the field of view of the radars. In open-pit mines with wide-open areas, the approach might fail due to too few existing objects in the environment.

Evans and Eagen (2021) and Rizos et al. (2011) use a constellation of ground-based transmitters, called Locata, to augment the navigation solution in open-pit mines. This approach can cover GNSS-denied areas but expects the vehicles to have line of sight to a certain number of transmitters. As the mining site changes continuously, the position of each transmitter has to be chosen wisely.

Schölderle et al. (2010) give an alternative approach for precision farming. Although the application is different, the hardware used is interesting for mining applications. Their multi-sensor setup consists of a GPS receiver, an optical speed sensor that measures the longitudinal vehicle speed, and a yaw rate sensor. The sensor measurements are fused in a Kalman filter. The authors achieved good results, but neither the algorithm used is further stated nor is the setup tested in GNSS-denied environments.

The presented approaches are suitable for many applications. However, they are not well suited for the localization of articulated dump trucks in open-pit mines. Contactless speed sensors that measure the slip-free lateral and longitudinal vehicle speed over ground may be promising aiding for localization in GNSS-denied environments for any type of land vehicle. No existing approaches that use such sensors are known to the authors—neither optical sensors nor Doppler radars.

### 3 | METHODOLOGY

The navigation filter is based initially on measurements of an inertial measurement unit (IMU) and is aided by GNSS observables. The tightly coupled navigation filter is implemented as an unscented Kalman filter (UKF). To meet the challenges in mining environments, we extend the filter to a multi-sensor navigation filter by aiding the navigation solution with a two-dimensional optical speed sensor (Correvit), providing measurements at 100 Hz. As the Correvit measurements strongly depend on the sensor mounting angle, the misalignment angle is estimated online and considered in the update step of the UKF. Therefore, the state vector is extended with a new state representing the misalignment angle.

### 3.1 | Basis Navigation Filter

The navigation filter is implemented according to Konrad et al. (2018) and estimates 18 states:

$$\mathbf{x} = [\mathbf{p}_{eb}^e \mathbf{v}_{eb}^n \mathbf{q}_b^n \mathbf{b}_a \mathbf{b}_g c_b c_d]^T \quad (1)$$

where  $\mathbf{p}_{eb}^e$  is the three-dimensional position of the IMU body-frame origin in Earth-centered, Earth-fixed (ECEF) coordinates, and  $\mathbf{v}_{eb}^n$  is the three-dimensional velocity of the body frame with respect to the ECEF-frame in navigation frame (NED) coordinates.  $\mathbf{q}_b^n$  is a quaternion representing the alignment of the body frame to the navigation frame. The biases of the IMU,  $\mathbf{b}_a$  and  $\mathbf{b}_g$ , are also estimated and are therefore represented as three-dimensional vectors in the state vector. Since the filter is tightly coupled, the receiver clock error,  $c_b$ , and drift,  $c_d$ , are estimated. The coordinate system notation and rotation are based on Groves (2013).

The navigation filter is implemented as UKF. The filter uses a 6-DOF nonlinear discrete-time state-space model to estimate the 18 states:

$$\mathbf{x}_{k+1} = \mathbf{f}_k(\mathbf{x}_k, \mathbf{u}_k) + \mathbf{G}_k \mathbf{w}_k \quad \mathbf{w}_k \sim \mathcal{N}(0, \mathbf{Q}) \quad (2)$$

where  $\mathbf{x}_k$  is the state vector of the system at time step  $k$ . A strapdown algorithm propagates the state vector according to Wendel (2011), here represented by the nonlinear discrete-time state transition function,  $\mathbf{f}_k$ . The transition function propagates the IMU bias states using a random walk process, according to Petovello (2003). The receiver clock error and drift are modeled as a first-order Gauss-Markov process according to Breuer et al. (2016).  $\mathbf{u}_k$  is the input vector summarizing the IMU measurements, accelerations,  $\tilde{\mathbf{f}}_{ib}^b$ , and rotation rates,  $\tilde{\boldsymbol{\omega}}_{ib}^b$ . The matrix  $\mathbf{G}_k$  is the shape matrix and maps in each step  $k$  the process noise,  $\mathbf{w}_k$ , to the state vector,  $\mathbf{x}_k$ . The system noise is modeled as zero-mean Gaussian distribution with  $\mathbf{Q}$  being the covariance matrix. A separate measurement model integrates each aiding sensor into the filter:

$$\mathbf{z}_k = \mathbf{h}_k(\mathbf{x}_k) + \mathbf{v}_k \quad \mathbf{v}_k \sim \mathcal{N}(0, \mathbf{R}) \quad (3)$$

where  $\mathbf{z}_k$  represents the estimated measurements at time step  $k$ .  $\mathbf{h}_k$  is the nonlinear measurement function that models the relation between the states and the measurements.  $\mathbf{v}_k$  is the normally distributed zero-mean noise, with  $\mathbf{R}$  being the covariance matrix of the measurement noise.

Figure 1 gives a schematic representation of the navigation filter. The filter is executed at a rate of 100 Hz, as this rate corresponds to the sample rate of the IMU measurements,  $\tilde{\mathbf{f}}_{ib}^b$  and  $\tilde{\boldsymbol{\omega}}_{ib}^b$ . The GNSS correction step uses pseudoranges,  $\tilde{\rho}$ , and deltaranges,  $\tilde{\mathbf{v}}_{rel}$ , of GPS and Galileo satellites from one antenna. The position,  $\tilde{\mathbf{p}}_{eb}^e$ , and heading,  $\tilde{\psi}$ , of the dual-antenna GNSS receiver are used to calculate the initial state vector. A preprocessing step processes pseudoranges from a reference station received via mobile connection to perform differential corrections.

The GNSS measurements are subject to a varying communication and processing delay. Breuer et al. (2016) present an approach that utilizes the receiver's pulse per second (PPS) and a ring buffer to store past state vectors. The calculated delay is used to perform the UKF update on the corresponding past state vector and subsequently performs the necessary number of strapdown propagation steps until the current time is reached.

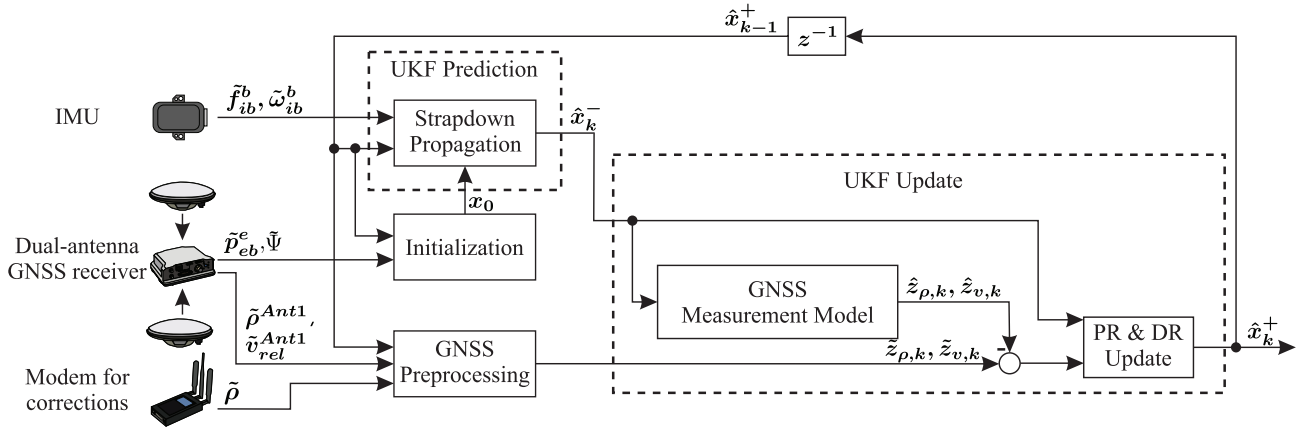


FIGURE 1 Schematic depiction of the navigation filter based on Gehrt et al. (2019): Variables with a hat symbol are estimated values, whereas the tilde indicates measurements.

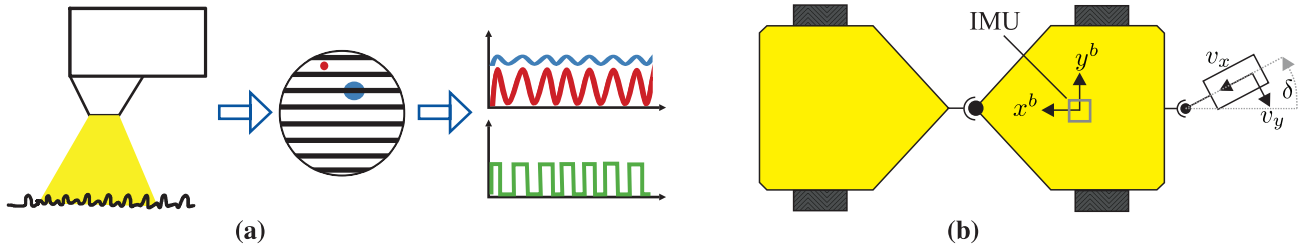


FIGURE 2 a) is a schematic depiction of the Correvit sensor functionality according to Haus and Lauinger (2007) while b) is a schematic illustration of the sensor mounting in top view.

## 3.2 | Optical Speed Sensor

### 3.2.1 | Measurement Principle

The speed sensor we use in this project is the Kistler Correvit S-Motion DTI. It is a two-axis optical sensor used for precise slip-free measurements of distance traveled, speed, and slip angle in dynamic vehicle testing. The sensor is pointing downwards, and the movement of the traversed surface is projected onto an optical lattice. The surface structure generates an alternating photocurrent with a speed-proportional frequency. A processing unit subsequently calculates the speed and streams the data over the controller area network (CAN). Figure 2(a) illustrates the working principle. This measurement principle works best on stochastically structured surfaces like concrete, tarmac, or loose subsoil present in mines (Haus & Lauinger, 2007). The sensor has a speed range of  $\pm 250$  km/h and a distance resolution of  $<0.1$  mm. The measurement rate is set to 100 Hz. The sensor requires a distance to the ground of  $350 \pm 100$  mm. Due to the optical measurement principle, a certain operating threshold exists above the sensor that provides valid data. At speeds lower than 0.6 m/s, the measurement data is not considered valid and, therefore, is not used to aid the navigation filter. Two different speed measurements are available as CAN messages: the raw measurements produced by the optical measurement principle and speed values from an internal sensor fusion. We decided to use the raw data instead of the fused data, as no information about the sensor fusion and the time correlation of the data was available.

### 3.2.2 | *Sensor Mounting*

We decided to attach the sensor to the trailer hitch. Figure 2(b) shows an illustration of the sensor mounting in the top view. The used mounting keeps the sensor xy-plane perpendicular to the ground but does not allow accurate alignment around the z-axis. Due to a possible mounting error, the sensor coordinate systems of the Correvit and the IMU are not perfectly aligned. Not considering this misalignment error,  $\delta$ , would result in a drifting position solution, as fractions of the longitudinal speed will appear in the lateral speed output of the sensor and vice-versa.

### 3.2.3 | *Discussion*

A navigation filter processes sensor measurements in both the propagation and the update step. In this section, we justify the integration of the Correvit as an additional update step. Farrell (2008) assumes that measurement updates should be performed with a rate lower than the propagation rate of the filter. Groves (2013) specifies that the update rate should not exceed the propagation rate and, like Wendel (2011), gives a computational load reduction as the only reason. Since the computational load is sufficient in the present project, the multi-sensor navigation filter can be implemented with a high-rate sensor in the update step. One further reason against the use of the Correvit in the propagation step is the availability of the measurement data. The propagation step should have new measurement data at each sample step since this step is the basis of the filter and must operate robustly. The optical measurement principle is error-prone, whereas the IMU failure probability in harsh mining environments is assumed to be significantly lower. Correvit failures can occur, e.g., due to insufficient structures in the traversed ground, although this case can almost be excluded. The sensor speed threshold, due to the measurement principle, further supports this decision.

## 3.3 | *Filter Extension for Speed Sensor Integration*

### 3.3.1 | *Measurement Model*

We integrate the Correvit into the tightly coupled navigation filter with an additional two-dimensional measurement equation. To account for the misalignment error, we introduce a new state,  $\delta$ , into the state vector, which represents the misalignment angle around the Correvit z-axis:

$$\mathbf{x} = [\mathbf{p}_{eb}^e \ \mathbf{v}_{eb}^n \ \mathbf{q}_b^n \ \mathbf{b}_a \ \mathbf{b}_g \ c_b \ c_d \ \delta]^T \quad (4)$$

We neglect the lateral displacement of the sensor due to the misalignment since it is small compared to the lever arm from the IMU to the Correvit. The measurement model is:

$$\hat{\mathbf{z}}_{es,k}^s = \mathbf{C}_{s,k}^s \underbrace{[\mathbf{C}_b^s (\mathbf{C}_{n,k}^b \mathbf{v}_{eb,k}^n + \boldsymbol{\omega}_{ib,k}^b \times \mathbf{1}_s^b)]}_{\mathbf{h}_k(\mathbf{x})} + \mathbf{v}_{s,k}, \mathbf{v}_{s,k} \sim \mathcal{N}(\mathbf{0}, \mathbf{R}_s) \quad (5)$$

where  $\hat{\mathbf{z}}_{es}^s$  is the estimated two-dimensional speed measurement of the Correvit sensor frame (s) relative to the ECEF frame (e) given in the Correvit sensor frame.  $\mathbf{C}_n^b$  rotates the estimated velocity from the NED frame to the IMU body frame.

$\omega_{ib}^b \times \mathbf{1}_s^b$  accounts for lever arm effects during rotations where  $\mathbf{1}_s^b$  is the lever arm from the IMU to the Correvit sensor.  $\mathbf{C}_b^{\hat{s}}$  compensates the reversed y-axis of the Correvit compared to the IMU axis orientation as can be seen in Figure 2(b):

$$\mathbf{C}_b^{\hat{s}} = \begin{bmatrix} 1 & 0 \\ 0 & -1 \end{bmatrix} \quad (6)$$

Lastly,  $\mathbf{C}_s^{\hat{s}}$  rotates the estimated sensor output around the sensor z-axis by the estimated misalignment error,  $\delta$ .  $\mathbf{C}_s^{\hat{s}}$  is thereby a simple two-dimensional rotation matrix:

$$\mathbf{C}_s^{\hat{s}} = \begin{bmatrix} \cos(\delta) & -\sin(\delta) \\ \sin(\delta) & \cos(\delta) \end{bmatrix} \quad (7)$$

Figure 3 shows schematically the extended navigation filter. The filter performs the pseudorange and deltarange update, and after that, the Correvit update, if GNSS and Correvit measurements are available. If either of the measurements is unavailable, the corresponding update step is skipped. The state vector and covariance matrix are updated in the update blocks according to the UKF theory.

Combining a sensor that measures the longitudinal and lateral speed over ground and the measurement model ensures that the nonholonomic vehicle characteristics are considered in the filter. This is further discussed in Section 4.3.

### 3.3.2 | Modeling the Misalignment Angle

The misalignment error occurs when the sensor is mounted and does not change afterward. Therefore, the new state is, according to Groves (2013), a systematic time-invariant error and should be kept constant in the process model of the UKF. This assumption would hold for a perfectly modeled system. However, this is not the case for this navigation filter. The UKF could assign unmodeled faults, such as multipath, to the new state. By modeling as a constant error, the state is kept constant in the process model, which at the same time leads to  $Q_\delta$  being zero. In this case, the corresponding error covariance matrix entry,  $P_\delta$ , can only decrease, which is equivalent to an increase of the confidence in this state. If, during the convergence phase, unmodeled errors occur that the UKF could assign to this state,

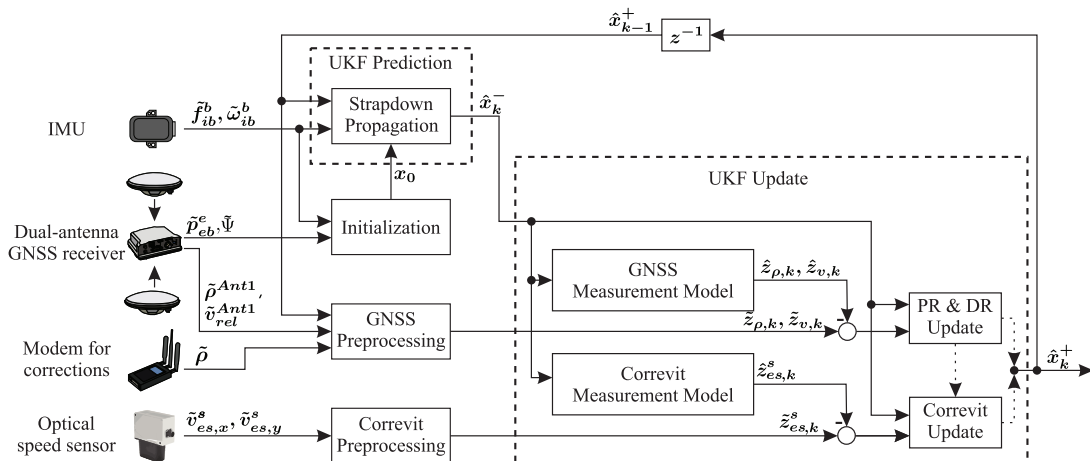


FIGURE 3 Final navigation filter with sequential measurement models

the errors cannot be compensated for later because of the possible high confidence in this state. To prevent this, we model the state as a random walk:

$$\underbrace{\dot{\delta}}_{\dot{x}} = \underbrace{0}_{f(x,u)} + \underbrace{I_{1 \times 1}}_G w_\delta \quad w_\delta \sim \mathcal{N}(0, Q_\delta) \quad (8)$$

with a normally distributed zero-mean process noise,  $w_\delta$ . As a result, the filter does not lose any degrees of freedom. This assumption is further analyzed in Section 4.2 with a closer look at the real filter behavior.

The Correvit update in the UKF is only executed if new measurements are available and either the lateral or the longitudinal speed measurement is greater than the threshold of 0.6 m/s. This is because the optical measurement principle provides invalid data at lower speeds. The misalignment error is only estimated if GNSS data is available; otherwise, the state is not observable. During GNSS outages, the corresponding error covariance matrix entry,  $P_\delta$ , is kept constant, as well.

At the set Correvit frequency of 100 Hz, the sensor indicates that the measurement delay is 6 ms. Therefore, the correction is applied to the previous state vector, and then the process model is applied to obtain the states at the current time step. Using the earlier explained ring buffer makes this implementation robust against various measurement delays.

### 3.4 | GNSS Preprocessing

The navigation filter uses pseudoranges and deltaranges from GPS and Galileo from a single antenna. In a preprocessing step, differential corrections are calculated using pseudoranges from a reference station received via a modem, implemented in Nitsch et al. (2021). If no correction data is available (e.g., during network connection outages), the correction method is replaced by dual-frequency methods or model-based methods, explained in more detail in Gehrt et al. (2018). Further steps in preprocessing are the calculation of satellite positions and velocities as the tightly coupled navigation filter needs them. Before using the preprocessed GNSS data, an integrity check is performed with the well-known receiver autonomous integrity monitoring (RAIM) algorithm, explained in more detail in Liu et al. (2019).

### 3.5 | Filter Initialization and Parameterization

The filter is initialized using the GNSS receiver outputs. Therefore, the initial position, speed, heading, clock bias, and drift are determined. The initial roll and pitch angle are computed based on accelerometer readings. The acceleration biases are set to zero in the initialization phase. The gyro biases are determined by averaging the gyroscope measurements over five seconds while the vehicle is not moving. The covariance matrices  $\mathbf{Q}$ ,  $\mathbf{R}$ , and  $\mathbf{P}$  are initialized as described in Breuer et al. (2016). We determined the covariance matrix of the Correvit,  $\mathbf{R}_{\text{Correvit}}$ , by a straight-ahead drive at constant speed on tarmac with the sensor x-axis pointing in the direction of travel. Since the sensor mounting does not allow mounting perpendicular to the direction of travel, we did not repeat the test with the y-axis pointing in the direction of travel. Instead, we assume that the longitudinal speed component's standard deviation also holds for the lateral speed component.

$$\mathbf{R}_{\text{Correvit}} = \begin{bmatrix} \sigma^2 & 0 \\ 0 & \sigma^2 \end{bmatrix} = \begin{bmatrix} 0.1092 & -0.0076 \\ -0.0076 & 0.1092 \end{bmatrix} \text{m}^2 / \text{s}^2$$

In this publication, we assume that the sensor noise is independent of the driven speed and the surface. This assumption is further discussed in the conclusion of this paper.

For the process noise variance,  $Q_\delta$ , of the new state,  $\delta$ , a small value is chosen as previously explained:

$$Q_\delta = 10^{-6} \text{ rad} \approx 0.0006^\circ$$

$Q_\delta$  is thereby a tuning parameter, which influences the convergence behavior of the misalignment angle. The state covariance is initialized with:

$$P_{0,\delta} = 0.1 \text{ rad} \approx 6^\circ$$

## 4 | EXPERIMENTAL VALIDATION

### 4.1 | Measurement Setup

The navigation filter presented in this publication was tested with a small articulated dumper. Figure 4 shows the measurement setup. The industrial-grade micro-electromechanical system (MEMS) IMU, a LORD MicroStrain 3DM-GX5-25, was mounted in a waterproof box in the middle of the vehicle and provided measurements via RS-232 at 100 Hz. The Correvit (Kistler S-Motion DTI) was attached to the trailer hitch. Speed measurements were available as CAN messages at 100 Hz. The GNSS receiver was a Novatel PwrPak7 dual-antenna receiver. It sent raw GNSS data over Ethernet with 10 Hz. The receiver utilized two Harxon GPS1000 survey antennas mounted on a rack with a sufficient baseline. The dual-antenna setup was used only for precise position and heading information to initialize the filter. The navigation filter processed the data of the antenna mounted on the right in the direction of travel. An Internet connection to receive differential data from the German SAPOS service was established with a Geneko GWR462-5W LTE router. A real-time programmable



FIGURE 4 One of the three research dump trucks from the ARTUS project with a rugged hardware attachment; all sensors are placed on the rear vehicle body. The illumination of the ground by the Correvit sensor is well recognizable.

logic controller (Bachmann MH230, VxWorks 7, Intel 2.3 GHz dual-core processor, 2 GB RAM) executed the navigation filter with all required modules with a sample time of 0.01 s. The PPS provided by the GNSS receiver was detected with one of the digital inputs of the Bachmann controller. Using the PPS, the communication and processing delays of the receiver were compensated for. The tests and evaluations were monitored with a notebook (Lenovo T480s, Windows 10, Intel 1.83 GHz quad-core processor, 16 GB RAM). As the IMU body frame was also the frame the state vector was specified in, the lever arms to the aiding sensors were of great importance:

$$\mathbf{l}_{Antenna}^b = [-0.10 \text{ m}, 0.54 \text{ m}, -1.62 \text{ m}]^T, \quad \mathbf{l}_{Correxit}^b = [-1.20 \text{ m}, 0 \text{ m}, 0.71 \text{ m}]^T$$

The lever arms were measured with a tapeline. However, the lever arms will be measured with a tacheometer for the pending test drives with the Bell e30 dump truck, as this vehicle is significantly larger. The vehicle speed was limited to around 5 km/h in the manual operation with remote control.

## 4.2 | Measurement Evaluation

We tested the multi-sensor navigation filter on a parking lot and in a gravel pit with the articulated dumper. We expected the extended filter to maintain position and heading accuracy for several seconds without GNSS. Furthermore, we expected that the new misalignment angle estimation (MAE) would further increase the filter performance during GNSS outages. To verify these expectations, we analyze the following three different filters. The first one is the basic UKF, the second one is the basic UKF extended with the Correxit measurement model, and the last one is the Correxit-aided UKF with MAE. The presented results were produced with recorded data in an offline postprocessing step since the MAE was implemented after the measurement campaign. The position, velocity, and heading solution of the Novatel PwrPak7D GNSS receiver serve as the ground truth. Figure 5 depicts a birds-eye view of the driven trajectories on the two test sites. Figure 6 shows the recorded raw Correxit speed measurements from the test on the parking lot. Due to the optical measurement principle, the raw signals are noisy. If the vehicle is not moving, the measured values are not noisy but exactly zero. The small peaks in the beginning result from a steering motion at a standstill.

The filter evaluation is split into four parts:

1. **Normal environmental conditions:** To analyze the performance of the three filters under the conditions that were present on the measurement day
2. **MAE performance:** Two different settings—estimation of the misalignment angle from the measurement setup and simulative rotation of the Correxit by  $5^\circ$
3. **Simulated GNSS cutoff:** To validate the filter performances in GNSS-denied environments, GNSS is disabled for 80 s.
4. **Gravel pit:** Test drive in a gravel pit with simulated GNSS interruption of 90 s

In the following, the results of the individual investigations are shown. Subsequently, the results are discussed in Section 4.3.

#### 4.2.1 | Normal Environmental Conditions

Figure 7 shows characteristic values to evaluate the behavior of the three navigation filters. Within the first seconds, the filter is not yet initialized, and therefore no error calculations are performed. The upper plot shows that the dumper drove at an almost constant speed of around 5 km/h during this test drive. The plot below shows the 2D position error. This is the Euclidean distance between the filter position and the reference position of the GNSS receiver without considering the height. It is noticeable that all filters have almost the same position error. In the beginning, the errors are, for a short time, above 0.5 m but then decrease. The mean 2D position error is equal for all filters with 0.22 m. The following plot shows the speed error. The magnitudes of the errors remain with the most time under 0.4 m/s. Interestingly, the speed update does not lead to any improvement in the speed estimation, even though the Correvit is a high-precision sensor. This is probably because the speed estimation already has a high quality due to the use of

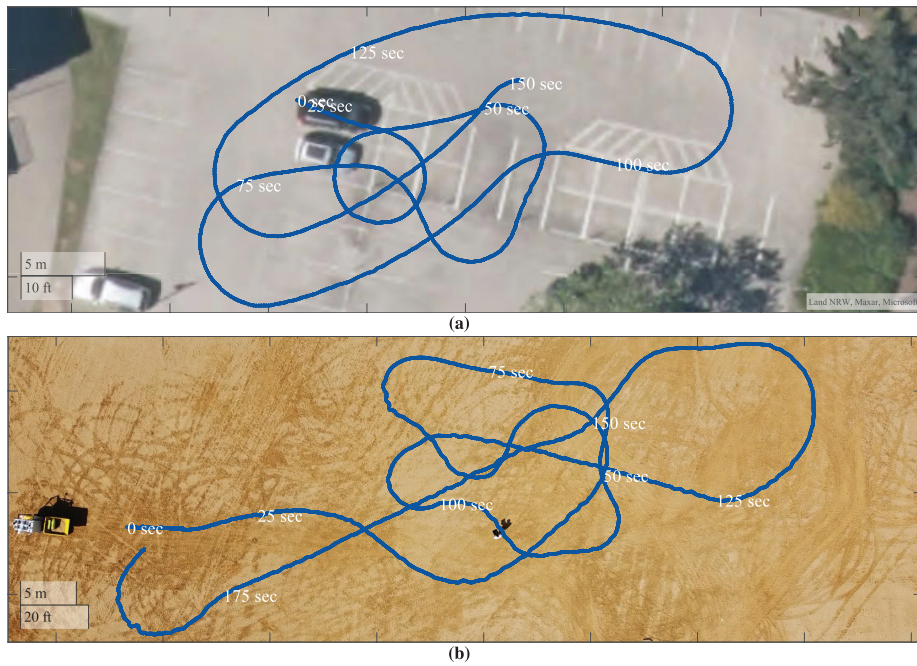


**FIGURE 5** Birds-eye view of the driven trajectory: a) test drive on a parking lot and b) represents evaluation in a gravel pit. The data belongs to the real-time kinematic (RTK) reference solution. The timestamps correspond to those of all other evaluation figures.

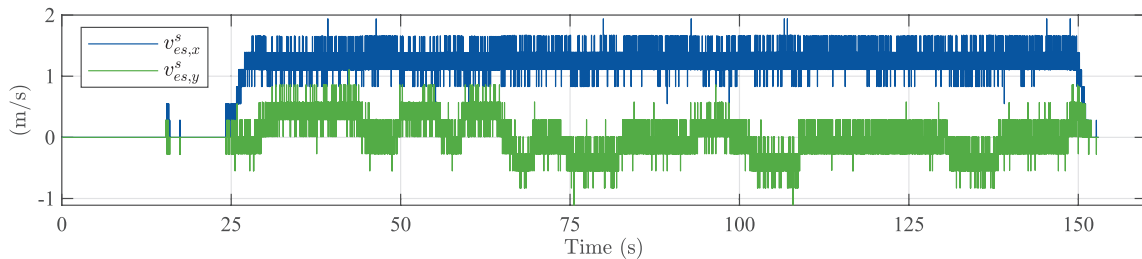


**FIGURE 6** Raw Correvit sensor output of the lateral and longitudinal speed component

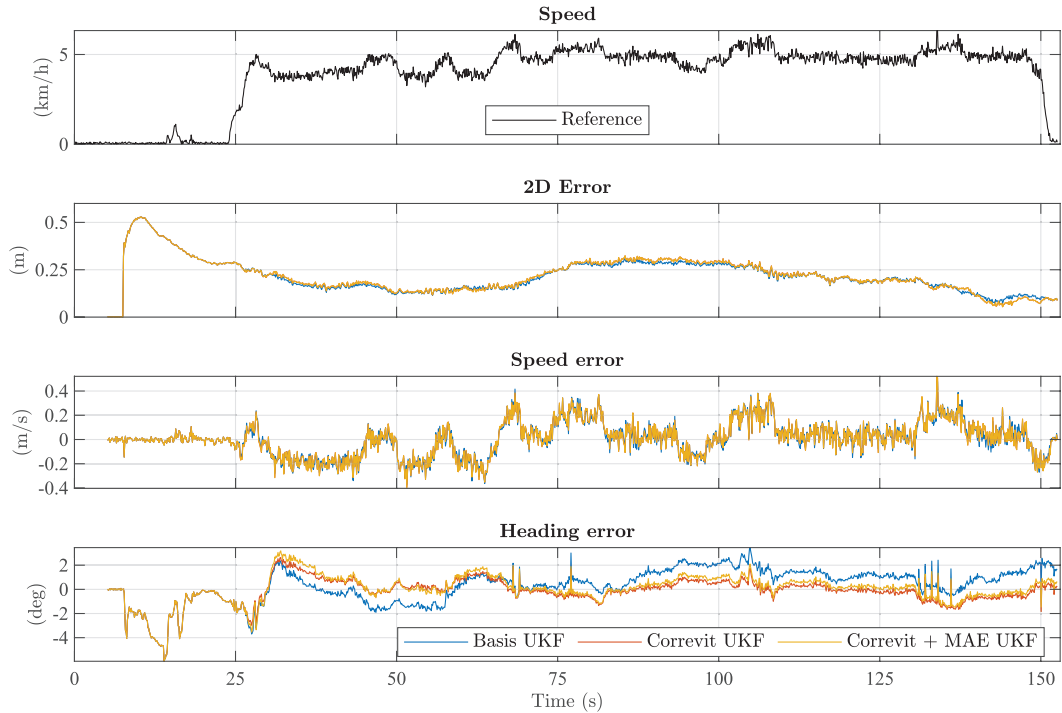


FIGURE 7 Comparison of the three navigation filters: basic UKF (without Correvet), Correvet UKF, and Correvet + MAE UKF

deltaranges in the filter. The last plot shows the error of the orientation estimation. In the beginning, the error is for all filters partly larger than  $5^\circ$ , but decreases as soon as the vehicle starts moving. This is because the heading is only observable when the vehicle is in motion. Right at the beginning, when the vehicle is at a standstill, this state has not yet converged in the filter. Both Correvet-aided filters performed slightly better than the basic UKF, whereas the filter without misalignment estimation performed the best with an average error of  $0.74^\circ$ . The spikes in the heading error plot occur because no reference data is available for these timestamps, and therefore, the error is calculated with data from previous time steps. Under optimal conditions, such as those present during the test drive, no significant differences can be seen between the basic UKF and the Correvet-aided ones.

#### 4.2.2 | Misalignment Angle Estimation Performance

The MAE is validated with two different settings. At first, it is examined whether the filter can estimate the real misalignment error, and afterward, the Correvet output is rotated by  $5^\circ$  in simulation. Figure 8(a) shows the results from the MAE. At second 25.5, the driven speed exceeds the predefined threshold, and the Correvet update is performed for the first time. It takes only 35 s for the filter to bring the state in proximity to its probably true value of  $0.54^\circ$ . This value is the mean of the last 75 s of data. Here, only the probably true value is mentioned because the mounting angle error is so small that it cannot be measured reliably. For further verification, we rotated the Correvet output in the simulation. A misalignment angle of  $5^\circ$  is simulated by rotating the Correvet measurements with a rotation matrix before the data is processed in the filter. As the true misalignment angle is probably around  $0.5^\circ$ , the data is rotated only by  $4.5^\circ$ .

Figure 8(b) depicts the simulation results. Within almost the same time, the filter is able to estimate the angle. Since the results are satisfactory, the assumption made at the beginning of this publication can be considered to be correct. The MAE achieves good results when the state is modeled as a random walk instead of a systematic error.

### 4.2.3 | Simulated GNSS Cutoff

To see the real capabilities of the multi-sensor navigation filter, we disabled GNSS for 80 s in simulation. Figure 9 shows the results of the different filters. The gray area marks the period without any GNSS signal. All filters behave in the first 50 s unchanged compared to Figure 7. Then GNSS is disabled for all filters. The position of the basic UKF starts drifting immediately since the only aiding sensor is not available anymore. The 2D error of the basic UKF increases up to 201 m during the period without GNSS. On the other hand, the 2D errors of the Correvit-aided filters show no major changes. This also holds for the heading and speed error. The filter with MAE can increase the position and heading accuracy even a little further. After GNSS is turned back on, both Correvit-aided filters are disturbed for a short period but then return to their previous accuracy. The basic UKF needs more time to adapt to the new situation. The disturbance occurs as the GNSS provides absolute position information and, during the period without GNSS, possible state errors accumulated. In addition, activating or deactivating sensors with their corresponding measurement model in a Kalman filter always results in some disturbances. This is due to the different signal quality considered in the measurement noise covariance matrix,  $\mathbf{R}$ .

At the time when the GNSS cutoff starts, the Correvit misalignment angle has not yet converged (see Figure 8[a]). The angle is estimated to be  $0.15^\circ$  and is not further estimated (as described in Section 3.3.2). A value of  $0.15^\circ$ , instead of  $0.54^\circ$ , is still better than not considering the mounting angle. This results in slightly better filter performance.

The small heading error is also a result of the fast converging IMU biases in the first seconds of the test drive. This is also the reason why the basic UKF maintains good orientation despite diverging position. The plot at the bottom of Figure 9 depicts the angular rate bias from the z-axis of the IMU.

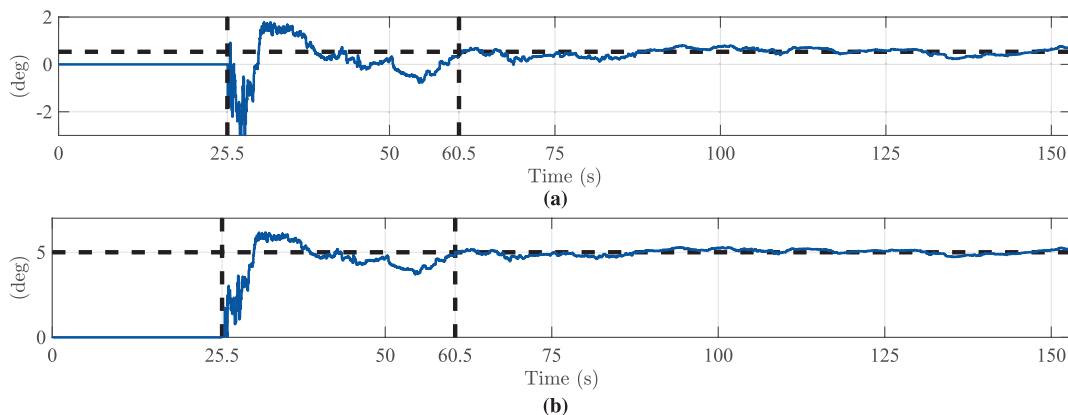


**FIGURE 8** Estimated misalignment angle  $\delta$ : The estimation starts after the vehicle begins moving at second 25.5. a) depicts the misalignment angle of the measurement setup while b) depicts a simulated misalignment angle of  $5^\circ$ . In both cases, the angle is estimated within 35 s.

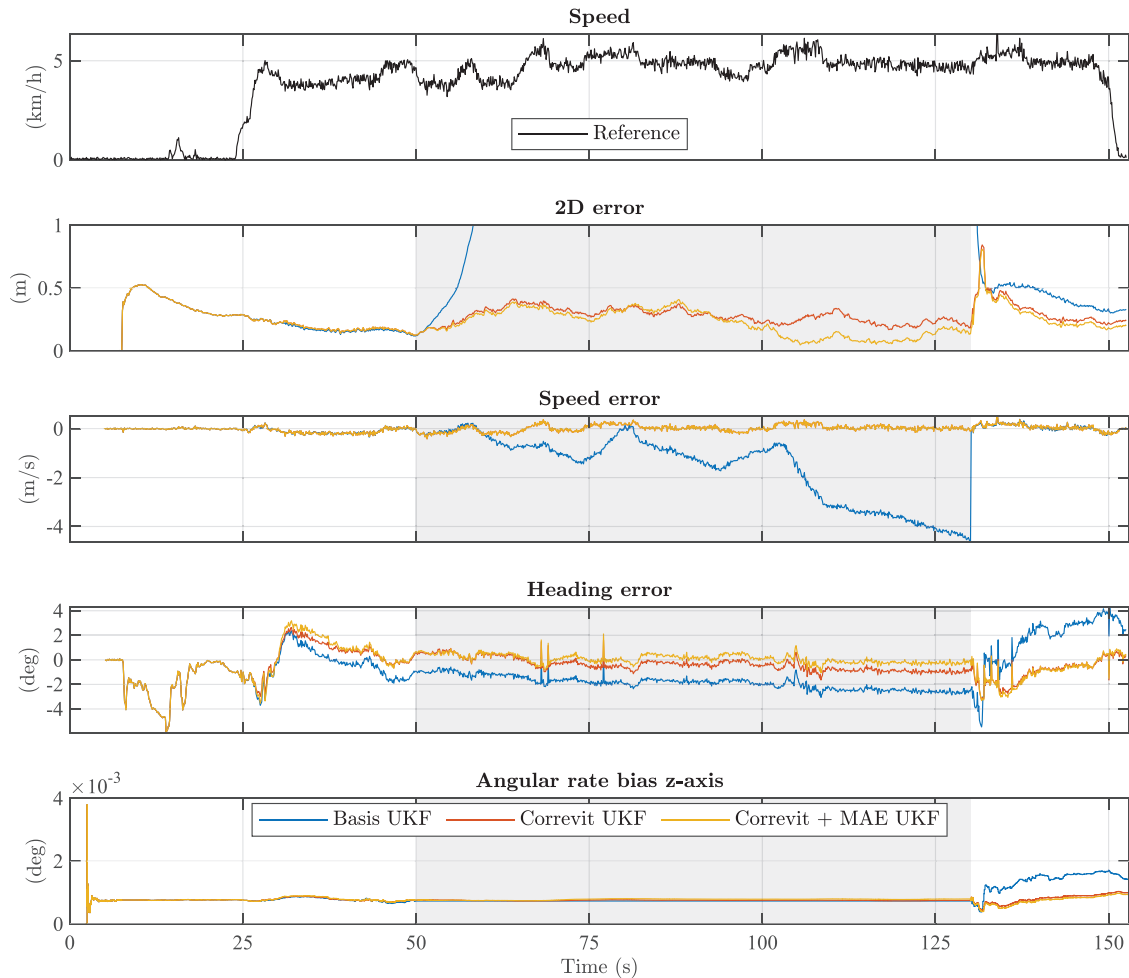
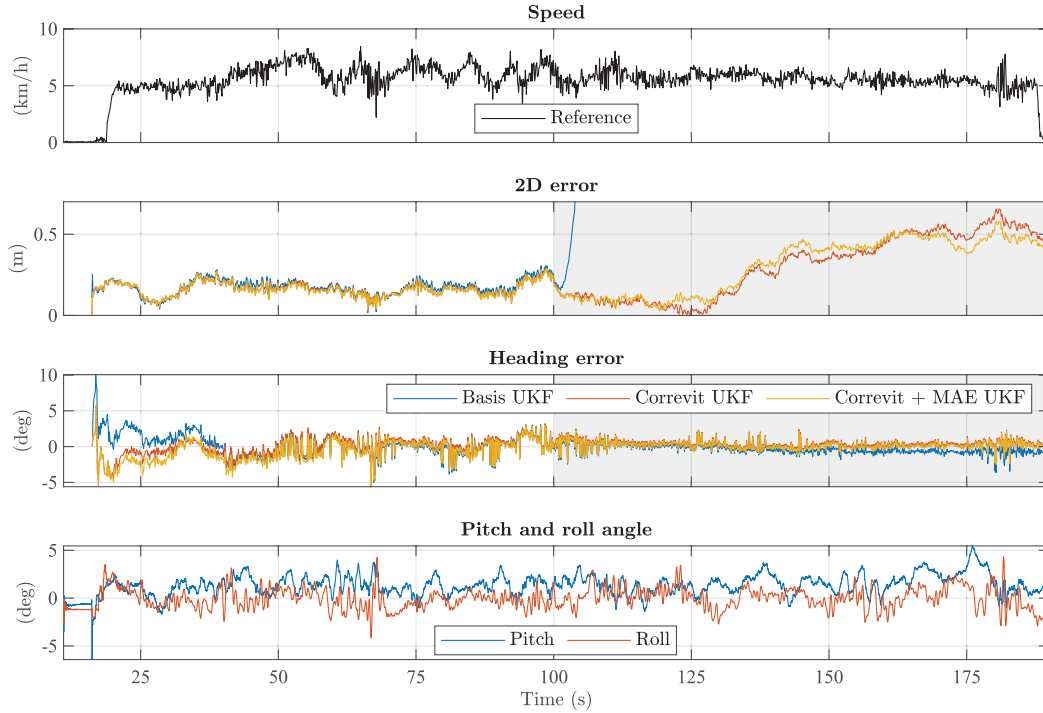


FIGURE 9 Comparison of the three navigation filters in offline postprocessing

#### 4.2.4 | Gravel Pit

The last test was conducted under more realistic conditions in a gravel pit. The surface was uneven with lots of potholes. As the gravel pit had perfect GNSS conditions, GNSS interruptions were produced manually. 100 seconds after the start, GNSS was turned off until the end of the test drive. The Correvit was remounted after transportation to the test site and had a new unknown misalignment angle. When GNSS was turned off, the misalignment angle was estimated to be  $-0.5^\circ$ . Figure 10 shows the results from the three filters. The speed was, again, almost constant at around 5 km/h. The uneven underground results in a noisy position and heading of the reference system which affects the error calculation. Until the GNSS interruption occurs, all filters have a position error below 0.3 m. After switching off GNSS, the position error remains at this low level for some time and then increases slightly. The filter that is aware of the sensor misalignment performs worse in the beginning but slightly better at the end of the test drive. The noisy heading of the reference system due to the uneven underground results in spiky heading errors. The heading of all filters converge fast. No difference between the Correvit-aided filters can be seen. In combination with the rigid vehicle, the uneven underground results in fast-changing roll and pitch angles, as seen in the last plot.



**FIGURE 10** Comparison of the three navigation filters in offline postprocessing with the data from the test drive in the gravel pit

**TABLE 1**

Position and Heading Errors of the Three Offline-Evaluated Filters for all Presented Experiments

Filter	2D-error (m)				Heading error (°)			
	$\bar{x}$	$\sigma$	$\tilde{x}$	P <sub>99</sub>	$\bar{x}$	$\sigma$	$\tilde{x}$	P <sub>99</sub>
<b>Normal environmental conditions</b>								
Basic UKF	0.22	0.09	0.21	0.43	1.17	0.88	0.66	5.53
Correvit UKF	0.22	0.09	0.21	0.43	0.74	0.84	0.57	5.53
Correvit + MAE UKF	0.22	0.09	0.21	0.43	0.83	0.89	0.66	5.53
<b>Simulated GNSS cutoff</b>								
Basic UKF	37.86	56.88	0.79	192.88	1.8	1.04	1.66	5.53
Correvit UKF	0.26	0.08	0.25	0.46	0.89	1.07	0.52	5.53
Correvit + MAE UKF	0.23	0.11	0.22	0.44	0.96	1.11	0.57	5.53
<b>Open-pit mine</b>								
Basic UKF	85.37	145.35	0.37	555.67	0.92	0.89	0.69	3.64
Correvit UKF	0.24	0.16	0.18	0.6	0.77	0.72	0.56	3.76
Correvit + MAE UKF	0.24	0.14	0.17	0.52	0.86	0.88	0.55	4.11

Note:  $\bar{x}$ : mean value,  $\sigma$ : standard deviation,  $\tilde{x}$ : median, P<sub>99</sub>: 99th percentile

### 4.3 | Discussion

The most important error values from all tests are summarized in Table 1. Under normal conditions, the position error is the same for the three filter configurations. However, the integration of the speed sensor significantly improves

the heading estimation. This could be due to inherent nonholonomic constraints in the speed sensor measurement model. The speed sensor also measures lateral speed. Since the articulated vehicle is a nonholonomic system, it cannot perform any desired lateral motion. Therefore, the measurements reflect the nonholonomic constraints of the vehicle and incorporate them into the measurement model. It could be seen as a zero-velocity update in the lateral direction whenever there is no slip. The filter without MAE achieved a slightly better estimation of the heading. One reason for this is that the MAE filter also uses erroneous angles in the convergence phase. This is reflected in the standard deviation and median. The heading error reaches its maximum absolute value in the first seconds after filter initialization for all filters. Therefore, the 99th percentile of the heading error is not informative.

In the 80-s period without GNSS, the basic UKF cannot estimate the position reliably. The heading, on the other hand, hardly deteriorates. This is due to the industrial-grade MEMS gyroscope. The Correvit-aided filters show, in this case, their actual performance. The experiment shows that the measurements from the speed sensor bound the speed error and keep the position error within certain limits for a certain GNSS outage time. Hardly any difference can be seen between the position error values and the first test drive with GNSS. The filter that considers the misalignment angle provides the best results because the performance depends on high-quality measurements. No matter how small the angle correction towards the actual mounting angle is, it will improve the result. The accuracy of the heading estimation is within the range of the results from the filter under normal conditions. The filter that estimates the misalignment angle performs slightly worse than the normal Correvit-aided one. This has to be further validated with longer test drives where the GNSS interruption occurs after all states have converged. The standard deviation of the position and heading of the Correvit + MAE UKF is slightly worse for the same reason as in the test drive with normal environmental conditions.

In a more realistic scenario in a gravel pit, the speed sensor enables position accuracy to be maintained for a long time in the absence of GNSS signals. The MAE does not bring any visible added value. One possible explanation could be the following: The uneven underground results in undesired roll and pitch angles. These fast-changing angles affect, through the matrix  $\mathbf{C}_n^b$ , the estimated Correvit measurements. As the fast changes in the roll and pitch angles are greater than the misalignment angle, the effect of the misalignment estimation and compensation is minor. Therefore, the position and heading of the MAE filter is not better than it was on tarmac.

Our assumption that the speed sensor noise can be considered constant has provided good results. With regard to the application scenario of the navigation filter, however, this assumption must be investigated in more detail since the ground can vary considerably in mining environments. An adaptive filter that permanently adjusts the measurement covariance matrix of the Correvit,  $\mathbf{R}_{\text{Correvit}}$  could already be a solution for this.

The multi-sensor navigation filter performs well under normal conditions and in GNSS-denied environments. During the phase with no GNSS, the Correvit-aided filters are able to maintain a smooth position. The basic UKF, on the other hand, drifts away after only a few seconds without GNSS. In general, it cannot be said that the angle estimation provides any added value. The positive effect seems to depend strongly on the environmental conditions. With more extended data sets, the MAE could be further investigated.

## 5 | CONCLUSION

In the publication on hand, a new tightly coupled multi-sensor navigation filter was presented, which was used in the project ARTUS to provide the trajectory controller of the articulated dumper with highly accurate and robust localization information. In open-pit mines, the reception of satellite signals may be severely restricted or not possible at all. To achieve robust vehicle localization despite the difficult conditions, we introduced a new filter update step utilizing high-rate 2D speed measurements from an optical speed sensor. The speed sensor was used to aid the filter permanently but mainly during long periods without GNSS. As the alignment of the speed sensor in the direction of travel was not perfectly possible, we extended the navigation filter with a misalignment angle estimation. Results from two test drives with an articulated dumper are shown. The new filter update estimated the misalignment angle within 35 s during one test drive. The multi-sensor navigation filter kept the position and heading accuracy over 80 s without GNSS with almost no visible decrease during a test drive on a parking lot. The test in a harsher environment has shown that the position error grows only slightly over time, but is still within acceptable limits. The mean position error was 0.24 m, and the heading error was  $0.77^\circ$  during the test drive in a gravel pit with a 90-s GNSS interruption. Due to the excellent performance, the presented filter can provide high-accuracy vehicle state information during critical maneuvers in the absence of GNSS. To make the setup more robust for use in open-pit mines, other sensors that measure lateral and longitudinal speed, e.g., Doppler radars, can be integrated into the presented framework. In future work, we will apply the introduced concept to a Bell e30 articulated dump truck with a load capacity of 28 tonnes and test it in an open-pit mine under actual mining conditions. The MAE could also be improved in future work. A rigid one could replace the variable mounting. The misalignment angle could then be estimated once in a calibration process or, with the proposed approach, keep it fixed after a certain convergence criterion is met. To further validate the Correvit-aided navigation filter, we plan to compare our approach with traditional wheel encoder-based odometry. Despite the promising results of the Correvit-aided filters, further test drives over several minutes or even longer with different GNSS failures have to be conducted in order to make a detailed statement about the navigation filter performance. The simulated GNSS interruptions were good for first evaluation steps but more challenging environments with multipath effects and single signal interruptions will show the real performance of the navigation filter.

## ACKNOWLEDGMENTS

This article is based mainly on the ION ITM 22 conference paper of the same name (Benz et al., 2022).

This work was supported by the German Federal Ministry of Education and Research in the research project ARTUS (grant 033R126DN).

## REFERENCES

- Benz, D., Gehrt, J. -J., Zweigel, R., & Abel, D. (2022). Speed sensor-aided navigation filter for robust localization in GNSS-denied mining environments. *Proc. of the 2022 International Technical Meeting of the Institute of Navigation*, Long Beach, CA, 1457–1468. <https://doi.org/10.33012/2022.18194>
- Breuer, M., Konrad, T., & Abel, D. (2016). High precision localisation in customised GNSS receiver for railway applications. *Proc. of the 29th International Technical Meeting of the Satellite Division of the Institute of Navigation (ION GNSS+ 2016)*, Portland, OR, 779–787. <https://doi.org/10.33012/2016.14696>

- Evans, M. J., & Eagen, S. E. (2021). Positioning performance in deep pit mines using GNSS augmented with Locata. *Proc. of the 2021 International Technical Meeting of the Institute of Navigation (ION ITM 2021)*, 295–306. <https://doi.org/10.33012/2021.17834>
- Farell, J. (2008). *Aided navigation: GPS with high rate sensors*. McGraw-Hill.
- Gehrt, J. -J., Konrad, T., Lin, J., Breuer, M., Abel, D., & Zweigel, R. (2018). High precision localisation with dual-constellation for railway applications. *Proc. of the 2018 International Technical Meeting of the Institute of Navigation*, Reston, VA, 35–45. <https://doi.org/10.33012/2018.15570>
- Gehrt, J. -J., Nitsch, M., Abel, D., & Zweigel, R. (2019). High accuracy navigation filter with dual antenna enabling double-differencing with dual-constellation. *Proc. of the 32nd International Technical Meeting of the Satellite Division of the Institute of Navigation (ION GNSS+ 2019)*, Miami, FL, 2186–2197. <https://doi.org/10.33012/2019.16917>
- Groves, P. (2013). *Principles of GNSS, inertial, and multisensor integrated navigation systems* (Second ed.). Artech House.
- Haus, J., & Lauinger, N. (2007). Optische gitter: die abbildung der realität – 75 jahre berührungslose dynamische meßtechnik auf der basis optischer gitter. *Laser Technik Journal*, 4(2), 43–47. <https://doi.org/10.1002/latj.200790155>
- Kellner, D., Barjenbruch, M., Klappstein, J., Dickmann, J., & Dietmayer, K. (2014). Instantaneous ego-motion estimation using multiple Doppler radars. *2014 IEEE International Conference on Robotics and Automation (ICRA)*, Hong Kong, China. <https://doi.org/10.1109/ICRA.2014.6907064>
- Konrad, T., Gehrt, J. -J., Lin, J., Zweigel, R., & Abel, D. (2018). Advanced state estimation for navigation of automated vehicles. *Annual Reviews in Control*, 46, 181–195. <https://doi.org/10.1016/j.arcontrol.2018.09.002>
- Liu, S., Gehrt, J. -J., Abel, D., & Zweigel, R. (2019). Dual-constellation aided high integrity and high accuracy navigation filter for maritime applications. *Proc. of the 2019 International Technical Meeting of the Institute of Navigation*, Reston, VA, 762–774. <https://doi.org/10.33012/2019.16723>
- Nitsch, M., Gehrt, J. -J., Heyn, L., Zweigel, R., & Abel, D. (2021). Embedded tightly coupled INS/DGPS-DGAL navigation filter on a mass-market single-board computer. *2021 International Conference on Localization and GNSS (ICLGNSS)*, Tampere, Finland. <https://doi.org/10.1109/ICL-GNSS51451.2021.9452196>
- Petovello, M. G. (2003). *Real-time integration of a tactical-grade IMU and GPS for high-accuracy positioning and navigation* [Doctoral dissertation, University of Calgary]. <https://doi.org/10.11575/PRISM/23031>
- Rizos, C., Lilly, B., Robertson, C. F., & Gambale, N. (2011). Open cut mine machinery automation: going beyond GNSS with Locata. *Proc. of the 2nd International Future Mining Conference*, Sydney, Australia. [https://unsw-primo.hosted.exlibrisgroup.com/primo-explore/fulldisplay/unswworks\\_modsunsworks\\_52899/UNSWORKS](https://unsw-primo.hosted.exlibrisgroup.com/primo-explore/fulldisplay/unswworks_modsunsworks_52899/UNSWORKS)
- Scheding, S., Dissanayake, G., Nebot, E. M., & Durrant-Whyte, H. (1999). An experiment in autonomous navigation of an underground mining vehicle. *IEEE Transactions on Robotics and Automation*, 15(1), 85–95. <https://doi.org/10.1109/70.744605>
- Schölderle, F., Zeimet, P., & Kuhlmann, H. (2010). A multi-sensor system in precision farming for position steered seed of sugar beet: an approach to the turnaround. *2nd International Conference on Machine Control and Guidance*.
- Wendel, J. (2011). *Integrierte navigationssysteme: sensordatenfusion, GPS und inertielle navigation* (Second ed.). Oldenbourg Wissenschaftsverlag. <https://doi.org/10.1524/9783486705720>
- Yang, B., Xue, L., Fan, H., & Yang, X. (2021). SINS/Odometer/Doppler radar high-precision integrated navigation method for land vehicle. *IEEE Sensors Journal*, 21(13), 15090–15100. <https://doi.org/10.1109/JSEN.2021.3071181>

**How to cite this article:** Benz, D., Gehrt, J. -J., Zweigel, R., & Abel, D. (2023). Speed sensor-aided navigation filter for robust localization in GNSS-denied mining environments. *NAVIGATION*, 70(1). <https://doi.org/10.33012/navi.566>